

Article

# Coherent Exciton Dynamics in Ensembles of Size-Dispersed CdSe Quantum Dot Dimers Probed via Ultrafast Spectroscopy: A Quantum Computational Study

Hugo Gattuso <sup>1</sup>, Barbara Fresch <sup>2</sup> , Raphael D. Levine <sup>3,4</sup> and Françoise Remacle <sup>1,\*</sup> 

<sup>1</sup> Theoretical Physical Chemistry, Research Unit Molecular Systems, University of Liege, 4000 Liege, Belgium; hgattuso@uliege.be

<sup>2</sup> Department of Chemistry, University of Padova, via Marzolo, 1, 35131 Padova, Italy; barbara.fresch@unipd.it

<sup>3</sup> The Fritz Haber Research Center, The Hebrew University of Jerusalem, Jerusalem 91904, Israel; rafi@fh.huji.ac.il

<sup>4</sup> Department of Molecular and Medical Pharmacology, David Geffen School of Medicine and Department of Chemistry and Biochemistry, University of California, Los Angeles, CA 90005, USA

\* Correspondence: fremacle@uliege.be

Received: 20 January 2020; Accepted: 11 February 2020; Published: 15 February 2020



**Featured Application:** Our results on the quantum electronic dynamics of quantum dots pave the way to several applications in nanoscience. The large density of purely excitonic coherences occurring on a wide range of time scales can be controlled by selecting the mean size of the two quantum dots (QDs) used to build the dimer and adjust to applications, for example, to light harvesting and information-processing devices.

**Abstract:** Interdot coherent excitonic dynamics in nanometric colloidal CdSe quantum dots (QD) dimers lead to interdot charge migration and energy transfer. We show by electronic quantum dynamical simulations that the interdot coherent response to ultrashort fs laser pulses can be characterized by pump-probe transient absorption spectroscopy in spite of the inevitable inherent size dispersion of colloidal QDs. The latter, leading to a broadening of the excitonic bands, induce accidental resonances that actually increase the efficiency of the interdot coupling. The optical electronic response is computed by solving the time-dependent Schrodinger equation including the interaction with the oscillating electric field of the pulses for an ensemble of dimers that differ by their size. The excitonic Hamiltonian of each dimer is parameterized by the QD size and interdot distance, using an effective mass approximation. Local and charge transfer excitons are included in the dimer basis set. By tailoring the QD size, the excitonic bands can be tuned to overlap and thus favor interdot coupling. Computed pump-probe transient absorption maps averaged over the ensemble show that the coherence of excitons in QD dimers that lead to interdot charge migration can survive size disorder and could be observed in fs pump-probe, four-wave mixing, or covariance spectroscopy.

**Keywords:** exciton dynamics; CdSe quantum dots dimers; size dispersion effects; coherent electronic dynamics; pump-probe transient absorption spectroscopy

## 1. Introduction

Colloidal nanometric metallic and semi conducting quantum dots (QDs) have long been used as versatile building blocks for assembling dimers and larger extended arrays [1–14]. Among possible building blocks, isolated CdSe QDs were extensively studied [15–19]. Driven by the possible

applications to lasing, sensing, light harvesting, and information processing, they have recently received renewed attention focusing on understanding the role of the fine structure coupling [20–24], electronic and vibrational coherences [25–32] and coupling to biexcitons [30,33–37], electron transport in arrays [38–41], and the possibility of engineering ultrafast energy transfer between a donor and an acceptor dot [10,11].

We focus in this paper on investigating theoretically coherent energy and charge transfer in ensembles of small (2 to 4 nm diameter) heterodimers and homodimers of CdSe QDs. The inevitable inherent size distribution of colloidal QDs leads to a distribution in electronic properties (exciton energies and wave functions and their couplings). For homodimers, where the dots are of equal mean radius, all excitonic bands of the two QDs make the dimer overlap. In the heterodimers, the sizes of the two QDs are tuned so that specific excitonic bands overlap, which favors efficient interdot coupling between those bands. Investigating the effects resulting from the size dispersion in the two dots that constitute a dimer is the main motivation of this paper.

The size effects on the optical properties of isolated nanocrystals were characterized early on [6,17,18,42–44]. A wide variety of theoretical approaches have been proposed to investigate the electronic properties of QDs of several hundreds to thousands of atoms [45,46]. Solid-state all atom density functional theory (DFT) computations have been implemented with adequate pseudo potentials using a direct diagonalization (DD) method [47–49]. One can also use the semi-empirical tight-binding (TB) atomistic approach based on a parametrized near neighbor Hamiltonian and a reduced number of basis orbitals to obtain electron and hole particles energies and wave functions [50–52]. For smaller dots, the exciton–phonon coupling has been investigated using a tight-binding surface-hopping approach [27,53,54]. For larger quantum dots in the range of 2 to 4 nm in diameter, parametrized model Hamiltonians based on the effective mass theory (EMA, single or multiband) and the  $\mathbf{k}\cdot\mathbf{p}$  method [18,55–58] provide valuable insights. The values of the parameters are determined by fitting experimental properties, in general, optical properties, or by extrapolating values obtained from atomic scale computations. While isolated CdSe QDs have been the subject of intensive research, up to now, only few modeling studies of dimers have been reported. They have mostly relied on the EMA model owing to the increased complexity and heavy computational cost of atomistic approaches for dimers [59–63].

Below, we use the EMA- $\mathbf{k}\cdot\mathbf{p}$  methodology [55] to describe the level structure of isolated 2 to 4 nm CdSe QDs and build an excitonic Hamiltonian for dimers. This approach allows computing the optical response of a large ensemble of QD dimers, taking into account the static disorder arising from the size dispersion in the optical response [26,28,64,65]. This inherent static disorder is typical of colloidal QDs and not present in ensembles of molecules that are only subject to the dynamical disorder induced by interactions with the environment. We specifically report on the fast tens of femtosecond charge migration and coherent energy transfer for ensembles of QD dimers excited by sequences of femtosecond laser pulses. The sequences of pulses used in the simulations are similar to the ones used to probe single dots by ultrafast pump-probe transient absorption spectroscopy [10,27,33,66–70] and in 2D electronic spectroscopy [25,26,28–32]. Ultrafast 10–30 fs intradot beatings of electronic coherences in single QDs with lifetimes in the range of 50–150 fs were reported using these experimental set-ups [25–32]. The dephasing time is ascribed to the coupling to environment, the effect of size dispersion, and the onset of coupling to the phonon modes, which span a wide range of time scales from 100 fs to several ps. Our simulations show that, when the interdot distance is sufficiently short and the QD diameters are adequately chosen, interdot electronic coherences have beating frequencies in the 10–30 fs range, and thus could be observed experimentally by ultrafast fs pump-probe spectroscopy before extensive dephasing owing to the coupling to environment and to the phonon modes kicking in. Building ultrafast fs electronic coherences in QD ensembles with fs laser pulse sequences is an ideal way to tune and manipulate the spatial and temporal localization of the electronic density before the onset of dephasing, an ability that is crucial for the development of light harvesting [71] and quantum information devices [59,72,73].

In Section 2, we outline the essentials of the EMA modeling for a dimer including both local and CT excitons. We systematically model the level structure of dimers as a function of the QD size and QD separation to be able to account for size dispersion and linker length. The effect of the size dispersion on the electronic structure of the dimer is analyzed in Section 3.1. The results on the coherent excitonic quantum dynamics of a QD dimer excited by a sequence of fs laser pulses are reported in Section 3.2. In Section 4, we show that the coherences can be probed at the level of the ensemble by pump probe femtosecond (fs) transient absorption spectroscopy. Conclusions and perspectives are given in Section 5.

## 2. Materials and Methods: Model Excitonic Hamiltonian

We consider isolated CdSe QDs with a radius between 1 and 2 nm. For such small QDs, one can assume a spherical symmetry. As the QD size is smaller than the bulk Bohr radius of the exciton, the strong confinement regime limit applies and the optical properties and the dynamics can be described in terms of the transition between quantized levels of holes and electrons in the confining potential. The potential is described as a spherical well of finite depth. For each dot, the EMA and  $\mathbf{k}\cdot\mathbf{p}$  parabolic expansion at the  $\Gamma$  point of the Brillouin zone provides a one particle Schrödinger equation for the radial envelope functions. Solving this equation gives the hole and electron energies and wave functions as a function of the QD size. The specific details and values of the parameters of the wells and of the effective mass for the hole and the electron for CdSe QD are given in the Supporting Information (SI, Section 1).

We investigate the fast, sub picosecond, dynamical response of large ensembles of QD dimers to sequences of fs laser pulses, focusing on the interdot excitonic coherences. To keep the computational cost reasonable, we use a minimal description of the electronic level structure of each QD. Band mixing [17,18,58] for the hole wave functions is not included. The fine structure arising from spin-orbit coupling of the hole wave function and from the crystal field and exchange splitting [17,18,20,21,58,74] is also neglected. As we focus on the short time, sub ps optical response, longer time picosecond relaxation processes such as the electron-phonon coupling [27,46,54,75,76], which is the result of non adiabatic coupling between the electronic and nuclear motion and the coupling to biexcitons, owing to weaker Coulomb interactions and Auger relaxation [30,33–37], are not included in our model.

We retain three single particle levels and wave functions per dot—see Figure 1A and Figure S1A of Section 1 of the SI—two holes, and one electron. The hole basis states are restricted to the two lowest states of the envelope function, 1S and 2S. The electron wave function is of 1S symmetry.

Once the energies and wave functions of the single particle (holes and electron) states have been determined, one can build an effective two particle (electron–hole) excitonic Hamiltonian  $\hat{H}_{he}(\mathbf{r}, \mathbf{r}')$ :

$$\hat{H}_{he}(\mathbf{r}, \mathbf{r}') = \hat{H}_h(\mathbf{r}) + \hat{H}_e(\mathbf{r}') + \hat{V}_{Coulomb}(|\mathbf{r} - \mathbf{r}'|) + E_{gap} \quad (1)$$

where the two one particle Hamiltonians  $\hat{H}_{h/e}(\mathbf{r})$  and their parameters are given in Section 1 of SI and  $E_{gap}$  is the value of the bulk band gap, see Figure 1A. Using these parameters, we obtain a good agreement with spectroscopic results in the range of QD diameter from 2 to 4 nm for the 1S exciton of isolated dots; see Figure S1B of SI Section 1.

The exciton basis functions are two-particle wave functions; in the strong confinement approximation, they are given as the product of the hole and the electron wave function solutions of  $\hat{H}_{h/e}(\mathbf{r})$ :

$$\phi_k^{he} = \phi_{ij}^{he} = \phi_i^{h*}(\mathbf{r}_1, \sigma_1) \phi_j^e(\mathbf{r}_2, \sigma_2) \quad (2)$$

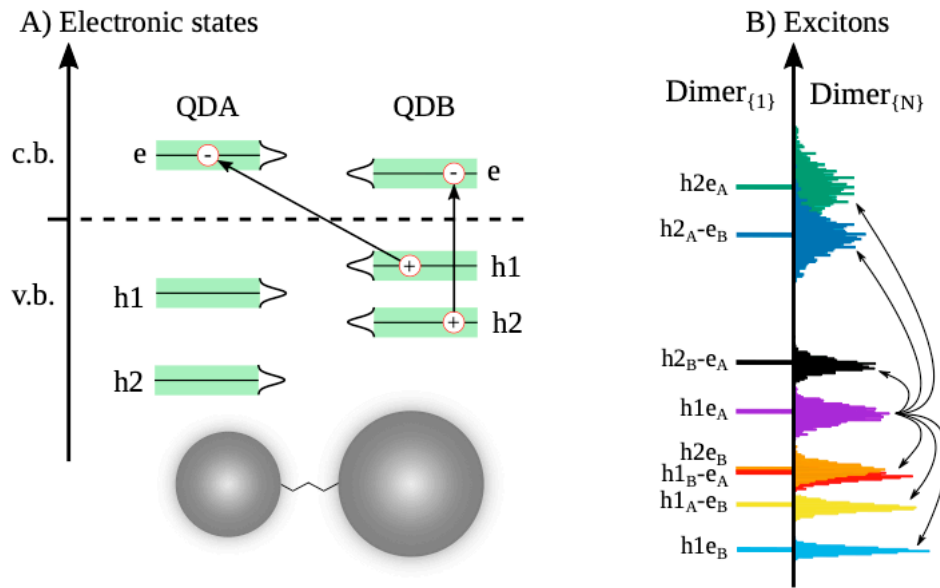


**Figure 1.** (A) The two hole and one electron single particle states considered in the model to build the excitonic level structure of a heterodimer. The arrows represent the two different kinds of excitations leading to excitons, a local exciton (hole and electron on the same quantum dot (QD), exciton  $h2e_B$ ) and a charge transfer one (CT) with the hole on  $QD_A$  and the electron on  $QD_B$  ( $h1_B-e_A$ ). c.b. and v.b. stand for conduction band and valence band, respectively. (B) The resulting excitonic level structure; left scale for an isolated dimer, right scale for an ensemble of  $N = 1000$  dimers, for which the size of  $QD_A$  and  $QD_B$  is drawn from a Gaussian distribution with a width,  $\sigma$ , of 5% in diameter ( $D_A = 2.25$  nm,  $D_B = 3.85$  nm). Because of the inherent size dispersion, each level of the single dimer (left) corresponds to an exciton band (right). For the two sizes shown in panel A, the  $h2e_B$  exciton band overlaps with the  $h1_B-e_A$  one. The arrows show the Coulomb coupling between the exciton  $h1e_A$  and the other excitons in the band. For the details on the Coulomb couplings between different types of excitons, see SI Section 3 and Figure S3; for details about the size distribution effects, see SI Section 5.

From two hole and one electron levels per QD, we obtain two local exciton states per QD, the ground state (GS) exciton  $1Se-1Sh_{3/2}$  and the first excited exciton  $1Se-2Sh_{3/2}$ , where  $i = 1Se$  and  $j = 1Sh_{3/2}, 2Sh_{3/2}$  in Equation (2). In this convention, the excitons are labelled by their electron and hole functions. In CdSe, the hole state is localized on Se and the lowest 1S and 2S hole states have angular momentum  $J = 3/2$ . The electron state is localized on Cd. With two exciton levels per QD, one can build eight zero order exciton states for the dimer. The excitation to which they correspond and the labeling used in the paper are shown in Figure 2, see also Figure 1. There are four local (Frenkel) excitons, two on  $QD_A$  and two on  $QD_B$ , labeled 1 to 4, and four charge transfer (CT) excitons for which the hole and the electron are not on the same QD, labeled 5 to 8. When the two dots are of different sizes, one obtains hetero donor-acceptor dimers.

The exciton basis corresponds to eight zero order singly excited electronic singlet states of the dimer. In the basis of the exciton antisymmetrized singlet basis functions, the matrix of the Hamiltonian (Equation (1)) takes the following form [35,77,78]:

$$H_{ij,i'j'} = (E_i^e - E_j^h)\delta_{ii'}\delta_{jj'} - J_{ij,i'j'} + K_{ij,i'j'} \tag{3}$$

with the Coulomb

$$J_{ij,i'j'} = \sum_{\sigma_1\sigma_2} \iint d\mathbf{r}_1 d\mathbf{r}_2 \phi_i^h(\mathbf{r}_1, \sigma_1)\phi_j^{e*}(\mathbf{r}_2, \sigma_2) \left( \frac{e^2}{4\pi\epsilon\epsilon_0|r_1 - r_2|} \right) \phi_{i'}^{h*}(\mathbf{r}_1, \sigma_1)\phi_{j'}^e(\mathbf{r}_2, \sigma_2) \tag{4}$$

and exchange integrals

$$K_{ij,i'j'} = \sum_{\sigma_1\sigma_2} \iint d\mathbf{r}_1 d\mathbf{r}_2 \phi_i^h(\mathbf{r}_1, \sigma_1) \phi_j^{e*}(\mathbf{r}_2, \sigma_2) \left( \frac{e^2}{4\pi\epsilon\epsilon_0|r_1 - r_2|} \right) \phi_{i'}^{h*}(\mathbf{r}_2, \sigma_2) \phi_{j'}^e(\mathbf{r}_1, \sigma_1) \quad (5)$$

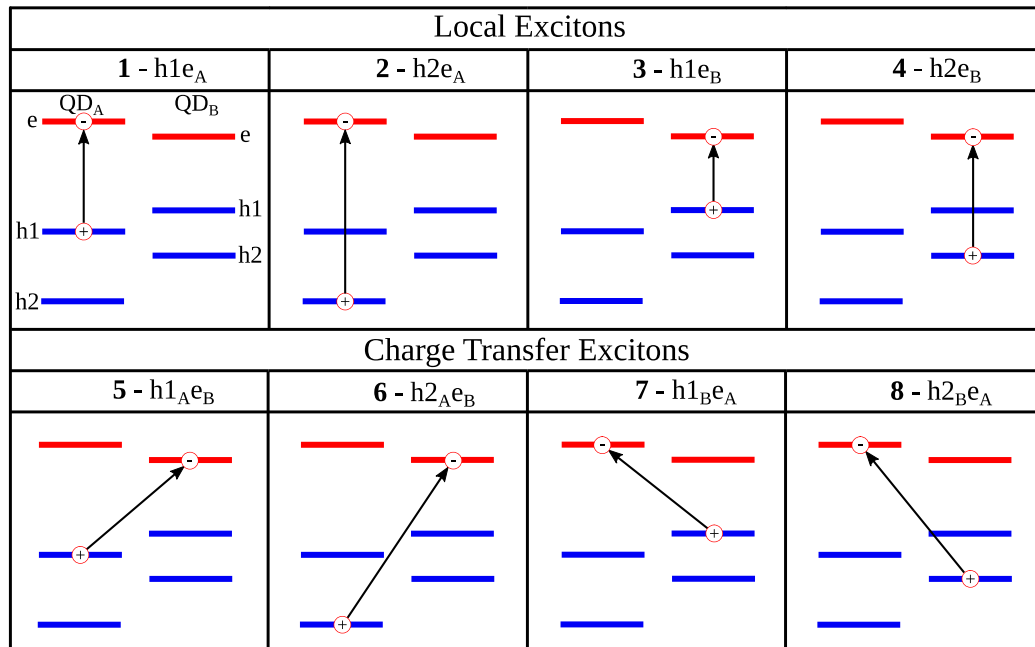


**Figure 2.** Schematic representation of the eight zero order exciton states taken into account in the model for a QDA–QDB dimer.

In a dimer, the Coulomb interactions  $V_{Coulomb}(|\mathbf{r} - \mathbf{r}'|)$  (Equation (1)) can either couple two single excitons localized on the same QD or couple the two QDs, see Figure S3, Section 3 of the SI. The two particle, six dimensional integrals (Equations (4) and (5)) are computed numerically using a double Monte Carlo integration scheme (see details in the SI Section 3 and Figures S4 and S5). The Coulomb integrals are screened by the dielectric constant of the material, see Section 3 and Figures S6 and S7 of the SI for details. Our numerical implementation for the computation of the Coulomb couplings was benchmarked with respect to known analytical expressions for particular Coulomb matrix elements [79]. We computed exciton coupling surfaces as a function of the dot radius (1 to 3 nm) for two QDs, QDA and QDB, in a dimer at fixed surface to surface distances (0.1 to 0.6 nm) by numerical integration. These surfaces were then fitted with simple analytical expressions, so that, when working with an ensemble, one can readily retrieve the coupling values for any given pair of QD radii or QD-to-QD distance. Examples of maps of coupling terms are given in Figure S8 (Section 3 of the SI) for local–local, local–CT and CT–CT exciton pairs. As we numerically computed the Coulomb integrals, we do not separate the local–local Coulomb matrix elements into short (Dexter) range and long (Föster) range interactions [80].

Solving the one particle Hamiltonian,  $\hat{H}_{e/h}(\mathbf{r})$ , for the electron and hole confined to spherical wells as a function of the QD radius provides the zero order excitonic structure necessary to build the matrix of the Hamiltonian for the dimer, Equation (3). In terms of electronic configurations, the non-coupled zero order excitons correspond to singly excited configurations. These are coupled by Coulomb interactions. The diagonalization of the electronic excitonic Hamiltonian, Equation (3), corresponds to a configuration interaction single (CIS) in terms of electronic states and provides the eigen excitons.

The size distribution (see Figure S10, Section 3 of the SI) leads to a dispersion in the one particle energies and wave functions, which in turn leads to a dispersion in the energies of the excitons and

in the Coulomb couplings. At the level of the ensemble, one obtains excitonic bands (see Figure 1B), which can be made to overlap by tuning the diameter of two QDs in the dimer. When bands of excitons overlap, accidental resonances play a role in increasing the effective strength of the Coulomb coupling. We focus on these aspects below and show that the coherent energy and charge dynamics of the dimer could be observed by transient absorption spectroscopy.

The magnitude of the different kinds of intra and interdot couplings governs the time scales of the coherence dynamics. In Figure 3, we report the intra and interdot coupling strengths for a heterodimer, with QD diameters  $D_A = 2.35$  nm and  $D_B = 3.85$  nm with 3% size dispersion, for two values of surface to surface distance,  $L$ , of  $L = 0.2$  nm, approximately corresponding to the S-CH<sub>2</sub>-S dithiol ligand (Figure 3A) and  $L = 0.55$  nm, corresponding to S-(CH<sub>2</sub>)<sub>3</sub>-S, Figure 3B. In Figure 3, Coulomb couplings (Equations (4) and (5)) are grouped according to the nature of the pair of zero order excitons involved and the intra or interdot character of the Coulomb coupling. The sizes of the two QDs are tuned to obtain a resonance in energy between the local exciton,  $h2e_B$  (exciton 4 in Figure 2) on the large dot, QD<sub>B</sub>, and the CT state  $h1_B-e_A$  (exciton 7), as shown in Figure 1B, which favors the otherwise weak interdot coupling through accidental resonances.

Qualitatively, the efficiency of inter dot Coulomb coupling depends on the overlap between the hole and electron wave functions localized on each QD separately, see Figure S2 in Section 1. The overlap is controlled by the surface to surface distance,  $L$ , and the exponentially decaying leakage of the hole and the electron wave functions outside of the QD, which decreases with the QD diameter. Therefore, the interdot couplings decrease with both the QD diameter (Figure S8, Section 3 of the SI) and  $L$ , as shown in Figure 3 for two  $L$  values. For a given size, the wave function of the electron,  $\phi_e(\mathbf{r})$ , is less confined than the hole wave functions and  $\phi_{h2}(\mathbf{r})$  is less confined than  $\phi_{h1}(\mathbf{r})$ .

The Coulomb couplings can be assigned to different groups based on the nature of the excitons involved and the range of energy they span. The intradot couplings as well as in the interdot local–local and diagonal Coulomb coupling for the CT states fall in the range of 0.1 to 0.01 eV (800 to 80 cm<sup>-1</sup>). The local–local interdot couplings fall in the 10<sup>-2</sup> to 10<sup>-3</sup> eV range depending on QD size and QD surface-to-surface distance. It decreases very little in the small range of center to center interdot distance ( $r_A + L + r_B$ ) spanned for the two values of  $L$  in Figure 3. This interdot coupling is of the order of the Coulomb coupling between zero order excitons localized on the same dot. On the other hand, interdot coupling strengths involving CT and local excitons are smaller, in the 10<sup>-3</sup>–10<sup>-4</sup> eV range, and fall exponentially with the interdot distance (see Figure S8 of the Section 2 of SI). The interdot CT–CT couplings are smaller than the local–CT ones (10<sup>-4</sup> to 10<sup>-6</sup> eV) and decay exponentially with interdot distance as well, except the coupling between states 5 ( $h1_A-e_B$ ) and 6 ( $h2_A-e_B$ ) and between 7 ( $h1_B-e_A$ ) and 8 ( $h2_B-e_A$ ), which are much larger. The reason is that, in each exciton involved in these particular coupling terms, the electron transfer goes in the same direction (from A to B for states 5 and 6 or for B to A for states 7 and 8, see Figure 2). In addition, these matrix elements involve an intradot Coulomb interaction between two hole states, which makes them stronger. As the energies of the two CT states involved in each pair differ by the intradot energy difference between the two hole states, even though the magnitude of the matrix element is large, this CT–CT coupling cannot lead to efficient coherent charge transfer in the dynamics. In general, because it is weak, the coupling between CT states leads to electronic coherences with very long periods, in the tens of ps. They are likely to be dephased by coupling to phonons and environmental effects, leading to trapping of charge and energy on a QD.

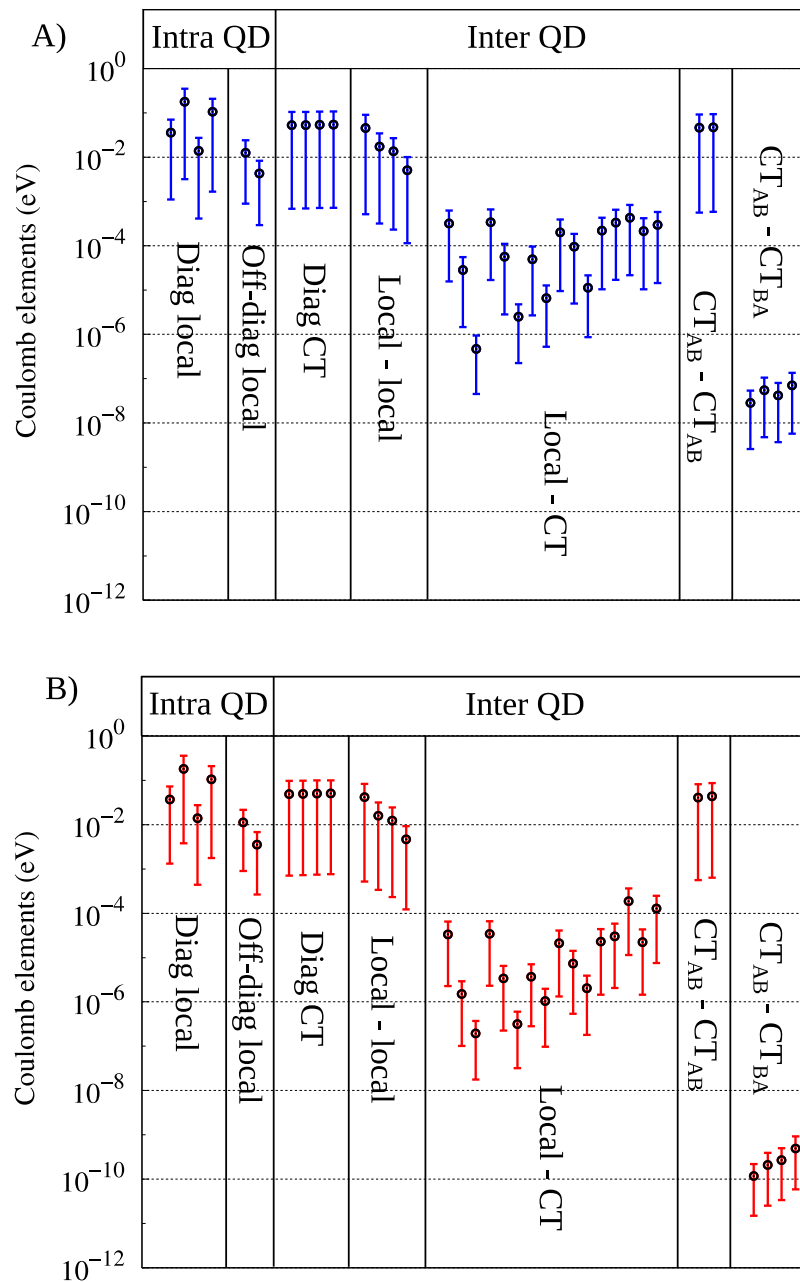


**Figure 3.** Absolute values of the Coulomb coupling strengths computed for a hetero dimer  $QD_A-QD_B$  ( $D_A = 2.35\text{nm}$ ,  $D_B = 3.85\text{ nm}$ ) on a logarithmic scale in eV for an ensemble of 1000 dimers with a size dispersion of 3% in diameter for two values of the surface-to-surface distance,  $L = 0.2\text{ nm}$  (A) and  $L = 0.55\text{ nm}$  (B). The black dots are the mean values and the bars the distribution of coupling strength values arising from the size dispersion. Note the wide range of couplings strengths, spanning about four orders of magnitude going from intradot coupling and interdot local–local couplings to interdot couplings between charge transfer (CT) excitons. ‘Diag’ and ‘off diag’ stand for the diagonal and off diagonal intra dot Coulomb matrix elements in the product basis, Equation (2). Interdot coupling also occurs between CT and local excitons and two CT excitons.

To summarize, interdot electronic coherences with fs periods are essentially the result of Coulomb interactions between two local excitons or between a CT and a local one. We show below that they could be observed at the level of the ensemble, explicitly taking into account the size dispersion.

To accurately describe electronic coherences with longer periods, one needs to take into account the coupling to the strong  $200\text{ cm}^{-1}$  phonon mode [27,64,65,81–83] and other dephasing processes.

Electronic coherence is built by exciting the ensemble of dimers with fs laser pulses. The excitons are coupled to the ground state (GS) and between them by the transition dipole matrix elements. The transition dipoles are non zero for pairs of excitons that differ at most by one particle wave function. There is a non zero transition dipole from the GS to all excitons, because an exciton corresponds to a singly excited singlet configuration. They are computed numerically for the eight GS to excitons and for the pairs of excitons for which an optical transition is allowed. For the small dots considered here, the transition dipole moments from the GS to the local excitons are found to increase essentially linearly with the QD diameter [84], and the transition dipole for the h2e exciton being about two times smaller than for the h1e one, see Figure S9, Section 3 of the SI. The dipole for the h1e transition varies between 28 D for a QD radius of 1 nm to 52 D for 2 nm [85] while the transition dipoles from the GS to the CT excitons are about 1000 times smaller (0.02 D) and decay exponentially with the interdot distance. In the computations below, the effect of the size dispersion on the one particle wave functions is taken into account when computing the dipole integrals. Upon diagonalization of the Hamiltonian, Equation (3), all eigenexcitons are endowed by an oscillator strength proportional to the mixing of the local and CT exciton by the Coulomb interactions.

### 3. Results

#### 3.1. Effect of the QD Size Dispersion on Excitonic Level Structure

In Figure 4, we show examples of the effect of the size dispersion on the energies of the zero order exciton levels (left) and of the eigen excitons (right) for ensembles of 1000 dimers of three different types: In panel A, a heterodimer built with  $QD_A$  and  $QD_B$  of mean diameters equal to  $D_A = 2.35\text{ nm}$  and  $D_B = 3.85\text{ nm}$  with 3% size dispersion and a surface to surface linker distance  $L = 0.2\text{ nm}$ . The two mean sizes were tuned so that the local exciton h2e<sub>B</sub> is isoenergetic with the CT exciton h1<sub>B</sub>-e<sub>A</sub>. In panel B, a heterodimer built with  $QD_A$  and  $QD_B$  of mean diameters of  $D_A = 2.7\text{ nm}$  and  $D_B = 3.5\text{ nm}$  with 5% size dispersion for  $L = 0.2\text{ nm}$ . In this case, there is no exact resonance between excitonic bands on each dot, but the bands h1e<sub>A</sub> and h2e<sub>B</sub> overlap, which leads to efficient interdot coupling between these two local excitons. In panel C, we show the level structure of the excitonic bands for a homodimer with a mean diameter of 2.5 nm, a size dispersion of 5%, and  $L = 0.55\text{ nm}$ . In the case of a homodimer, all the excitonic bands are resonant.

At the single particle level, the size distribution induces wider energy distributions for the small ( $QD_A$ ) dots than for the large ones ( $QD_B$ ), as expected because confinement effects are larger for smaller sizes. For the same reason, the energy distributions of the single particle levels are also wider for electrons than holes and for hole 2 than for hole 1, see Figure S2 of Section 1 of the SI. As a consequence, in a heterodimer where  $QD_A$  is smaller than  $QD_B$ , the confinement effects lead to wider energy distributions for the local h2e<sub>A</sub> and h1e<sub>A</sub> and for the CT h2<sub>A</sub>-e<sub>B</sub> excitons. From the random size distributions of the two QDs (see Figure S10, Section 5 of the SI), we obtain energy distributions of the zero order exciton that are also fitted to Gaussian distributions (Figure 4 left), with widths ranging from 10 to 80 meV depending on the type of excitation involved in each exciton. The values of the parameters of the Gaussian fits to the zero order energy distributions of the exciton for the QD parameters used in Figure 4A are given in Table S1. In addition to this intrinsic size dispersion effect, the exciton energy distribution will also be affected by environment effects, which we do not explicitly take into account here. The distributions of the coupling strengths also depend on the distribution of the one particle wave function. They are plotted for selected exciton pairs in Figure S11, Section 5 of the SI. Those of the transition dipole matrix elements are plotted in Figure S12 for the dimer with QD sizes of panel A. They also exhibit Gaussian distributions, and the parameters are given in Table S1.

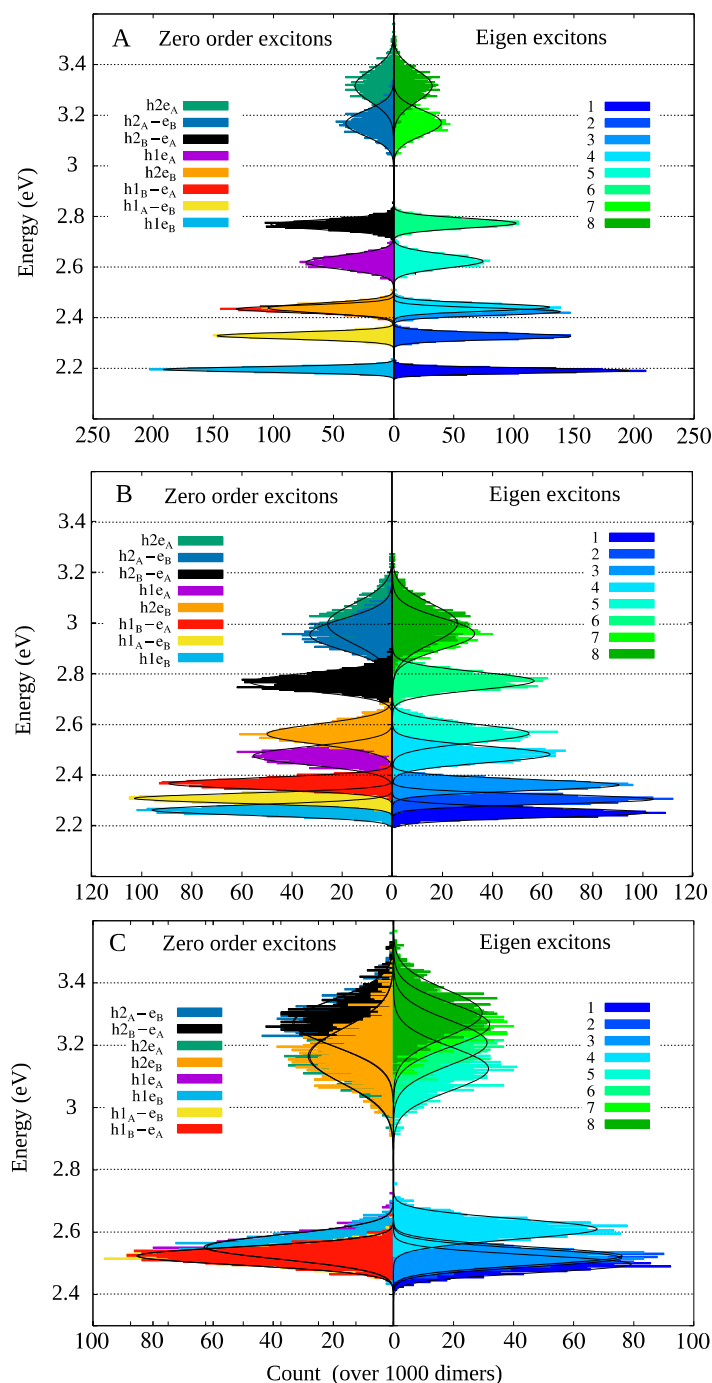


**Figure 4.** Dispersion of the energy levels of the zero order excitons (left) and of the eigen excitons (right) induced by size dispersion. The fits to Gaussian distributions are shown in black lines, see Table S1 of Section 4 of the SI for the Gaussian parameters. Computed for 1000 dimers of three different types. (A) A heterodimer with  $QD_A$  ( $D_A = 2.35$  nm) and  $QD_B$  ( $D_B = 3.85$  nm) with 3% size dispersion for the short  $L = 0.20$  nm ligand length. Note how the Coulomb interactions between the zero order exciton bands that overlap (exciton  $h2_B$  and  $h1_B-e_A$ ) lead to a splitting of the corresponding eigen exciton ones. (B) A heterodimer with  $D_A = 2.7$  nm and  $D_B = 3.5$  nm and  $L = 0.2$  nm and 5% dispersion in diameter. In this case, the exciton bands of the two local excitons  $h1e_A$  and  $h2e_B$  overlap. (C) Energies of the eigen exciton for a homodimer of QD with a diameter of 2.5 nm and  $L = 0.55$  nm. The size dispersion is 5% in diameter. All the bands overlap, but the splitting is small because  $L$  is larger, except for the higher energy exciton bands that involve the excitation of  $h2$  hole.

We can clearly see in Figure 4A left that the bands (centered at 2.44 eV) of excitons  $h2e_B$  and  $h1_{B-e_A}$  overlap and are well separated from the other pairs of excitons. There is also an overlap between the two exciton bands that involve the local exciton  $h2e_A$  and the CT one  $h2_{A-e_B}$ . For each of these bands, the effect of the Coulomb electronic coupling is enhanced because of accidental resonances. The sizes of panel B were engineered to be able to probe interdot coherences between local excitons and intradot ones. There is efficient coupling between the local exciton bands of  $h2e_B$  and  $h1_{e_A}$  (panel B left) that partially overlap, as well as between the higher exciton bands  $h2e_A$  and the CT one  $h2_{A-e_B}$ . For the homodimer (panel C), all the exciton bands overlap.

The zero order excitons are coupled by the Coulomb interactions, which also exhibit a dispersion in their strengths owing to the size dispersion effect on the wave functions (see Figure 3). The spectrum of the energies of eigenstates of the  $8 \times 8$  excitonic Hamiltonians of the 1000 dimers obtained by diagonalizing the Coulomb interactions are shown on the right hand side of panels A, B, and C of Figure 4. Overall, the distributions of eigen exciton energies remain Gaussian, which can be understood because the values of the Coulomb couplings are small. Compared with zero order, one observes a splitting of the two bands of excitons that were engineered to overlap,  $h2e_B$  and  $h1_{B-e_A}$  in panel A and of all the bands in panel C. The splitting is larger when the Coulomb interactions are large and the surface-to-surface distance between the QDs is small. In panel B, there is no significant splitting of the bands  $h1_{e_A}$  and  $h2e_B$  because they are not in exact resonance. However, because of the bands overlap, there are accidental degeneracies that increase the efficiency of the Coulomb coupling. This stronger effective coupling is responsible for a larger distortion of the zero order distribution, as can be seen in the values of the fits reported in Table S1. Typically, the bands of the two excitons that overlap at higher energy,  $h2e_A$  and  $h2_{A-e_B}$  in panels A and B, are less effectively coupled because the Coulomb interaction between these two excitons is smaller and there are less accidental degeneracies because these two bands are more spread in energy. On the other hand, in the homodimer (panel C), one observes a large splitting of the four higher energy bands that corresponds to the four excitons ( $h2e_B$ ,  $h2e_A$ ,  $h2_{A-e_B}$ ,  $h2_{B-e_A}$ ). Note that, in the case of the homodimer, the Coulomb interactions lead to a redistribution of the oscillator strength and break the rule of a purely bright and a purely dark eigen exciton, as would be the case for homodimers of molecules.

### 3.2. Coherent Excitonic Quantum Electronic Dynamics in the QD Dimer

The total Hamiltonian is time-dependent because it includes the dipole interaction between the electronic states of the QD dimer and the electric fields of the sequence of fs laser pulses used to pump and probe the ensemble. In the simulations reported below, we typically use two laser pulses: the first one to steer the coherent dynamics in the excitonic manifold and the second one for probing. The total electronic Hamiltonian is written as the sum of the field free dimer Hamiltonian,  $H_0$ , given by Equation (1) and the dipole coupling to the laser field:

$$\hat{H}(t) = H_0 - \mathbf{E}(t) \cdot \hat{\mu} \quad (6)$$

where  $\mathbf{E}(t)$  is the time-dependent electric field and  $\hat{\mu}$  is the dipole operator. We use as a basis set the eight excitons and the ground state. In the zero order exciton basis, the dipole interaction couples the ground state to all the exciton states, with the largest coupling to the local excitons. We neglect the Coulomb interactions between the GS and the excitons because the energy difference is large, larger than 2 eV, and the Coulomb coupling strengths are far smaller. In  $H_0$ , all zero order excitons are coupled by the Coulomb interactions (Equations (3)–(5)).

We compute the excitonic dynamics by numerically integrating the time-dependent Schrödinger equation (TDSE) using the Hamiltonian, Equation (6), expressed in eigenstates of  $H_0$  (the eigenexciton

basis) for each dimer in the ensemble. These states are stationary when there is no interaction with the laser pulse. In this basis set of nine electronic states, the wave function takes the form:

$$|\Psi(t)\rangle = \sum_{i=0}^8 c_i(t)|i\rangle \quad (7)$$

where  $i = 0$  is the GS and  $i = 1-8$  are the eight eigen exciton singlet states of each dimer. To solve the TDSE, we first transform the transition dipole matrix elements to the eigen exciton basis, which leads to a redistribution of the zero order oscillator strengths over all the eigen excitons. Then, the TDSE is integrated numerically:

$$i\hbar \frac{d\mathbf{c}}{dt} = \mathbf{H}(t)\mathbf{c} \quad (8)$$

where  $\mathbf{c}$  is the vector of the time-dependent amplitudes,  $c_i(t)$  of Equation (7). The time profile of the electric field for each laser pulse is confined by a Gaussian envelope:

$$\mathbf{E}(t) = \mathbf{E}_0 \cos(\omega t) \exp\left(-\frac{(t-t_0)^2}{2\sigma^2}\right) \quad (9)$$

In the simulations reported below, we use two pulses. The pump has a carrier frequency,  $\omega$ , of 570 THz (2.36 eV) in the visible ((VIS), tuned to excite the two local excitons  $h1e_A$  and  $h1e_B$  of the heterodimer shown in Figure 4B ( $=2.7$  nm and  $D_B = 3.5$  nm and  $L = 0.2$  nm and 5% dispersion in diameter) with similar amplitudes and generate an interdot electronic coherence. The pump field strength,  $E_0$ , is set to  $0.05 \cdot 10^9$  V/m ( $10^{-4}$  au of field, which corresponds to a peak intensity of  $3.3 \cdot 10^9$  W/cm<sup>2</sup>). The width of the pulse,  $\sigma$ , is 8 fs, which leads to an energy per pulse of about 0.50 nJ for a beam waist of 50 microns. We probe the electronic dynamics either with the same VIS pulse, or with an IR pulse ( $\omega = 100$  THz (0.41 eV),  $\sigma = 8$  fs,  $E_0 = 0.1 \cdot 10^9$  V/m ( $5 \cdot 10^{-4}$  au of field, peak intensity  $8.8 \cdot 10^9$  W/cm<sup>2</sup>).

We consider an ensemble of 1000 dimers with a random orientation of the molecular frame of the dimer with respect to the laboratory frame. The exciton quantum dynamics of each dimer in the ensemble is computed solving Equation (8). We begin by showing in Figure 5 the dynamics of a single heterodimer with  $D_A = 2.7$  nm and  $D_B = 3.5$  nm (see Figure 4B) and a short ligand ( $L = 0.2$  nm) in the zero order and in the eigenexciton basis set. For this heterodimer, as there is no exact resonance between two excitonic bands, the efficiency of the Coulomb coupling remains small and the eigenexcitons retain their labeling of the zero order basis. The VIS pump pulse essentially accesses  $h1e_A$  and  $h1e_B$ , with a small population in  $h2e_B$ . The probe IR pulse is applied 100 fs after the pump one. The dynamics can be analyzed in the basis of the zero order exciton states that are not stationary after the first pulse (panel A) or in the eigenexciton basis (panel B), which are stationary when no pulse is present. In the zero order basis set (Figure 5A), one observes population transfers between exciton  $h1e_A$  and  $h1e_B$  on a fast 17.9 fs time scale, as expected from the range of the Coulomb coupling strength shown in Figure 3A. The two corresponding eigenstates, 1 and 4, are stationary in the absence of pulse. The probe IR pulse leads to additional population transfer between the excitons. Its frequency is resonant with energy differences between intradot and interdot coherences. The dynamics of selected coherences between eigenexcitons,  $\rho_{ij}(t) = 2\text{Re}[c_i^*(t)c_j(t)]$ , where  $i$  and  $j$  are the two eigenexcitons involved in the coherence, are plotted in panels C and D. In the absence of pulse, each coherence has a beating frequency given by the energy difference ( $E_i - E_j$ ) between the two eigenstates  $i$  and  $j$ . In panel C, we plot the two intradot coherences between eigenexcitons having large weights on the local excitons  $h1e_A-h2e_A$  and  $h1e_B-h2e_B$  and, in panel D, the four interdot coherence between eigenexcitons having large weights on the four pairs of zero order local excitons that are strongly coupled:  $h1e_A-h1e_B$ ,  $h1e_A-h2e_B$ ,  $h1e_B-h2e_A$ ,  $h2e_A-h2e_B$ . We show the dynamics of the coherences between eigenexcitons because these are the ones probed by the probe pulse, and observed in the pump-probe transient absorption spectroscopy as reported below. The interdot  $h1e_A-h1e_B$  coherence (panel D) is the most intense interdot one, because the two

eigenexcitons are excited by the pump pulse. Its beating frequency corresponds to that of population exchange between the two zero order exciton involved in the coherence. This coherence is only weakly excited by the IR pulse, because its frequency is to the red of that of the IR pulse. On the other hand, the IR pulse excites the two intradot coherences and the other three interdot ones because it is resonant with their frequency. Coherences involving eigenexcitons having large weights on local and CT states have a much smaller amplitude. We show an example in Figure S13 of Section 6 of the SI.

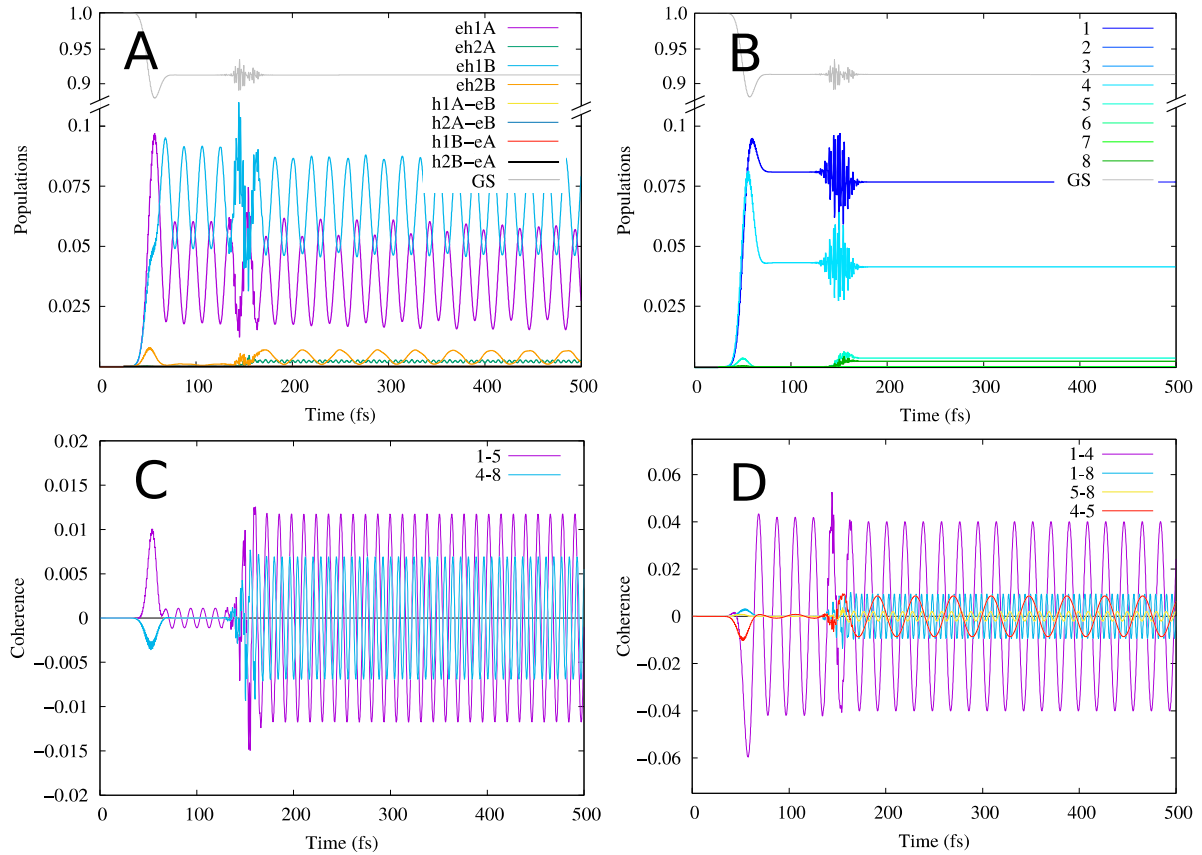


**Figure 5.** Dynamic of populations and coherences computed for a single heterodimer ( $D_A = 2.7$  nm and  $D_B = 3.5$  nm, level structure shown in Figure 4B) upon excitation by a sequence of the UV and the IR pulse with a delay time of 100 fs. (A). Population in the zero order excitons. (B) Population in the eigenexcitons. (C). Real part of the two intradot coherences. (D). Real part of the six interdot coherences between local excitons. GS, ground state.

#### 4. Discussion: Probing the Coherent Intradot and Interdot Dynamics in Dimer Ensembles

The coherences built by the first pulse can be probed by transient absorption (TA) spectra using a second pulse. We compute the transient absorption spectrum as the linear response function,  $S(\omega)$ , of the time-dependent oscillating dipole resulting from the coherent superposition of states that has been built by the pump pulse [86,87]. In the eigenstate basis, the time-dependent dipole of each dimer takes the following form:

$$\mu(t) = \text{Tr}[\hat{\mu}\rho(t)] = \sum_{k,l} c_k^*(t)c_l(t)\mu_{kl} = \sum_{k,l} \rho_{kl}(t)\mu_{kl} \quad (10)$$

where  $\mu_{kl}$  are the transition dipoles in the eigen exciton basis and the  $c_k(t)$ 's are the time-dependent amplitudes on the eigenstates (Equation (8)). Because of the electronic coherences,  $\rho_{kl}(t) = c_k^*(t)c_l(t)$ ,

the dipole is non stationary and beats in time with periods that correspond to the coherence periods. The transient absorption spectrum,  $S(\omega)$ , is defined as follows [82,83]:

$$S(\omega) = -2\text{Im}[\mu(\omega)E^*(\omega)] \quad (11)$$

where  $\mu(\omega)$  is the Fourier transform (FT) of the dipole given by Equation (10), including the interaction with the pump and the probe pulse; and  $E(\omega)$  is the complex conjugate of the FT of the time profile of the electric field of the two pulses, both computed for positive frequencies,  $\omega$ . Because  $\mu(t)$  and  $E(t)$  are real, their FTs obey the symmetry properties  $\mu(-\omega) = \mu^*(\omega)$  and  $E(-\omega) = E^*(\omega)$ . A positive value of the response function,  $S(\omega)$ , corresponds to an absorption process, while a negative value corresponds to emission.

Coherences with beating times spanning several orders of magnitude can be probed in the pump-probe transient absorption spectra. The beating frequencies of the coherences are defined by the energy differences between each pair of eigenstates,  $E_i - E_j$ . The beating of the phase of the coherence can be followed through the absorption/emission signals recorded when scanning the delay time between the pump and the probe pulses.

The transient absorption spectrum computed for an ensemble of 1000 hetero dimers  $\text{QD}_A\text{-QD}_B$  (mean  $D_A = 2.7$  nm, mean  $D_B = 3.5$  nm, size dispersion 5%) and  $L = 0.2$  nm is shown in Figure 6, superimposed with the energy distribution of the eigen excitons of the ensemble shown in Figure 4B. It is computed for a value of the delay time between the pump and the probe pulses,  $\tau = 100$  fs. The majority of the emission appears in the low energy side of each exciton band. When two identical VIS pulses (2.37 eV/570 THz) are used (panel A), the high transition frequencies in the 2 to 2.6 eV range, which corresponds to coherences between the local excitons and the GS, are resonant with the probe pulse and efficiently probed. However, the low transition frequencies between excitons are not resonant with the probe VIS pulse. An IR pulse (0.41 eV/100 THz) allows probing the exciton–exciton coherences, as shown in the inset of panel B. Because the carrier frequencies of the pump and the probe pulses used for computing the transient spectrum shown in panel B are markedly different, the signal in the high frequency range is the transient absorption spectrum induced by the pump, while the low frequency range shown in the inset is results from the probe. In panel A, the spectra attributable to the pump and the probe overlap.

Scanning the delay time,  $\tau$ , between the pump and the probe pulse provides direct access to the beating periods of the coherences. We present heatmaps of the transient spectra (Equation (11)) computed for the ensemble of 1000 dimers  $\text{QD}_A\text{-QD}_B$  ( $D_A = 2.7$  nm,  $D_B = 3.5$  nm,  $L = 0.2$  nm, 5% size dispersion) in Figure 7, where the  $x$  axis is the delay time  $\tau$  and the  $y$  axis the frequency axis of the spectra (ordinate of Figure 6). The color is blue for emission (negative value of the spectrum in Figure 6) and red for absorption (positive value in Figure 6). Panel A is computed for a sequence of two VIS pulses and panel B for a sequence VIS–IR. The coherences between the GS and the lowest excitonic bands  $h1e_A$  and  $h1e_B$ , called GS-1 and GS-4 in terms of their labeling in eigenexcitons, are excited by the pump and the probe and appear very clearly in the range 2.2 to 2.6 eV with the beating periods of  $\approx 2$  fs. The interexciton coherences (panel B) that fall in the 0.2 to 0.6 eV range are probed by the IR pulse. Their beating periods are longer, in the 10–20 fs range. They can have an intradot (band 1–5, corresponding to zero order excitons  $h1e_B$  and  $h2e_B$ , respectively, and band 4–8, corresponding to the  $h1e_A$  and  $h2e_A$  zero order exciton bands) or an interdot character (bands 1( $h1e_B$ )-4( $h1e_A$ ) and 5( $h2e_B$ )-8( $h2e_A$ )). The longer time scale interdot electronic coherences that involve weakly populated charge transfer states have periods in the dozens of fs range. They will eventually be coupled to the phonon and acoustic modes [24,78,79,84]. In Figure 8, we show the transient spectra computed for an ensemble of 1000 homodimers ( $D_A = D_B = 2.5$  nm,  $L = 0.55$  nm and 5% size dispersion). In this case, all the exciton bands overlap and the zero order labels are no longer valid. In panel A, the fast beating electronic coherences between the two bands of eigenexcitons, 1 and 4, and the GS are effectively probed by the VIS probe. Eigenexcitons 1 and 4 are formed by the coupling of the zero order excitons  $eh1_A$  and  $eh1_B$ . Their transition frequencies from the GS ( $y$  scale of the map) differ by about 0.15 eV,

which reflects the strength of the interdot Coulomb coupling. Their beating periods are of the order of 2 fs, as shown by their oscillations with respect to the delay time. In panel B, the IR pulse probes the coherence between the bands of eigenexcitons 4 and 5, whose beating frequency is resonant with the frequency of the IR pulse (0.4 eV). Eigenexcitons of band 4 have their main weights on the zero order excitons  $h1e_A$  and  $h1e_B$  and eigenexciton of band 5 on  $h2e_A$  and  $h2e_B$ . One can see from Figure 4C that these two eigen excitons are separated by  $\approx 0.4$  eV, which corresponds to a period of 10 fs along the delay time axis. This coherence has both an intra and interdot character.

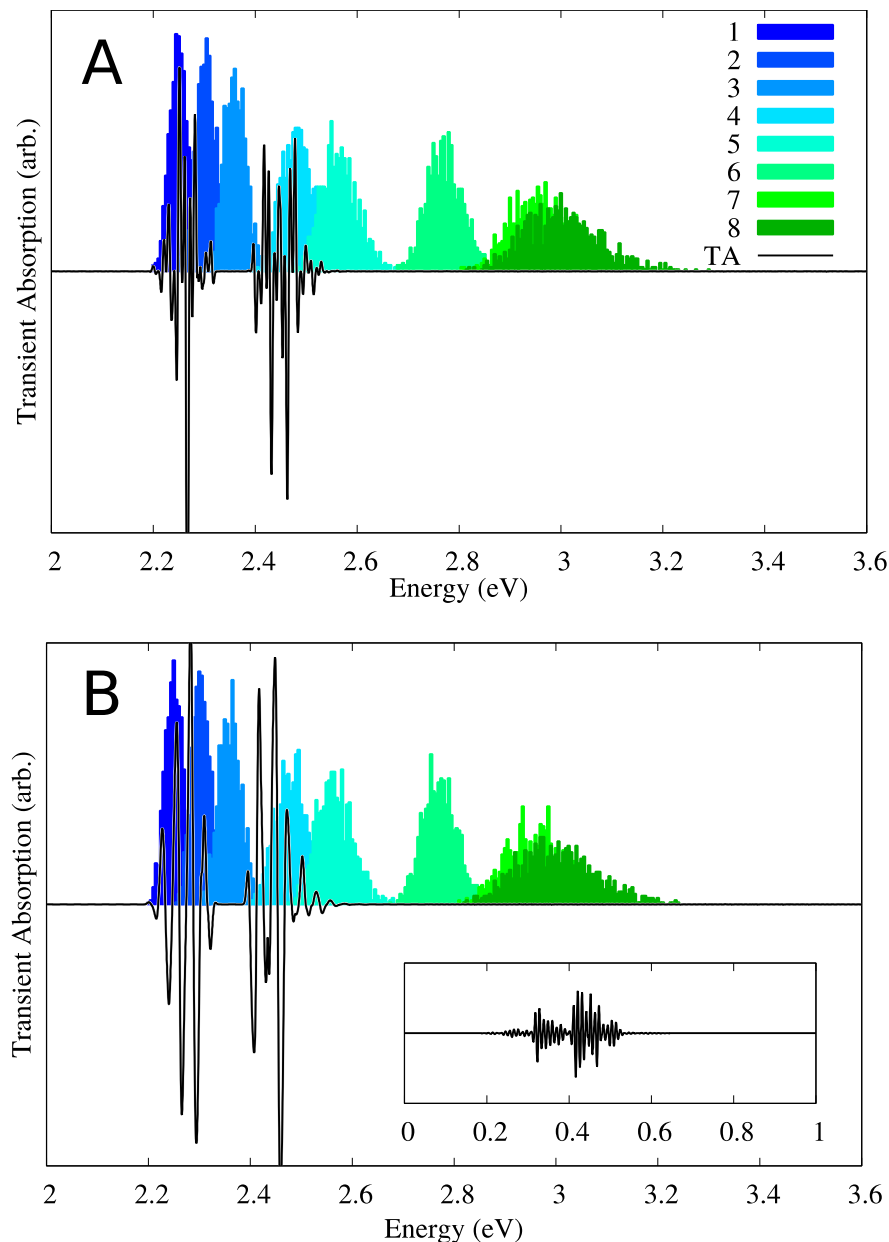


**Figure 6.** Transient absorption(TA) spectrum for an ensemble of 1000 heterodimer  $QD_A$  ( $D_A = 2.5$  nm) and  $QD_B$  ( $D_B = 3.7$  nm) (black) superimposed with the distribution of the energies of the eigenstates in GS to the exciton spectral region. (A). Computed for a sequence of two identical VIS pulses (2.37 eV, 570 THz,  $\tau = 100$  fs,  $t_{0\text{pump}} = 50$  fs,  $t_{0\text{probe}} = 150$  fs, the integration time is 2 ps) (B) Computed for a VIS-IR sequence (VIS: 2.37 eV, 570 THz,  $\tau = 100$  fs, IR: 0.41 eV/100 THz) where the IR probe is resonant with the low energy transition frequencies of the coherences between excitons. The inset shows the low frequency region on the same scale for the intensity.

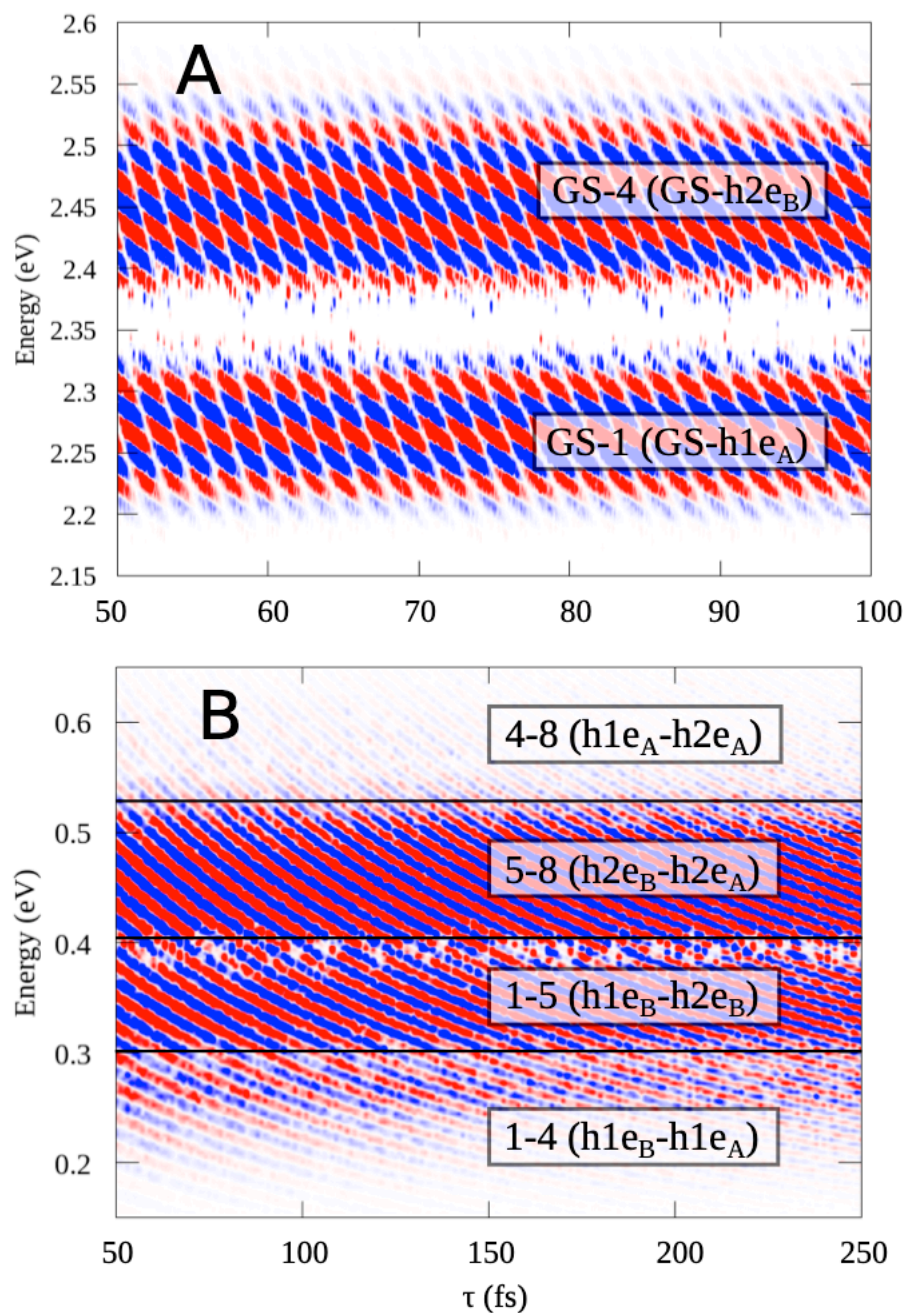


**Figure 7.** Heatmaps of the transient absorption spectra computed as a function of the delay  $\tau$  ( $x$  axis) between the pump and the probe pulses. The  $y$  axis is the frequency of the transient spectra. The color code corresponds to the intensity of the emission (blue, negative values) and of the absorption (red, positive values). (A) GS to exciton spectral region ( $y$  axis range from 2.0 to 2.6 eV) computed for delay times corresponding to fast coherence beatings on 2 fs time scale and a pulse sequence VIS–VIS. In this case, the second VIS pulse probes the eigenexciton bands GS-1 and GS-4. (B) The low frequency region of the  $y$  axis that is probed by the VIS–IR sequence of pulse, which probes the interdot and intradot interexciton electronic coherences, as labelled in the insets.

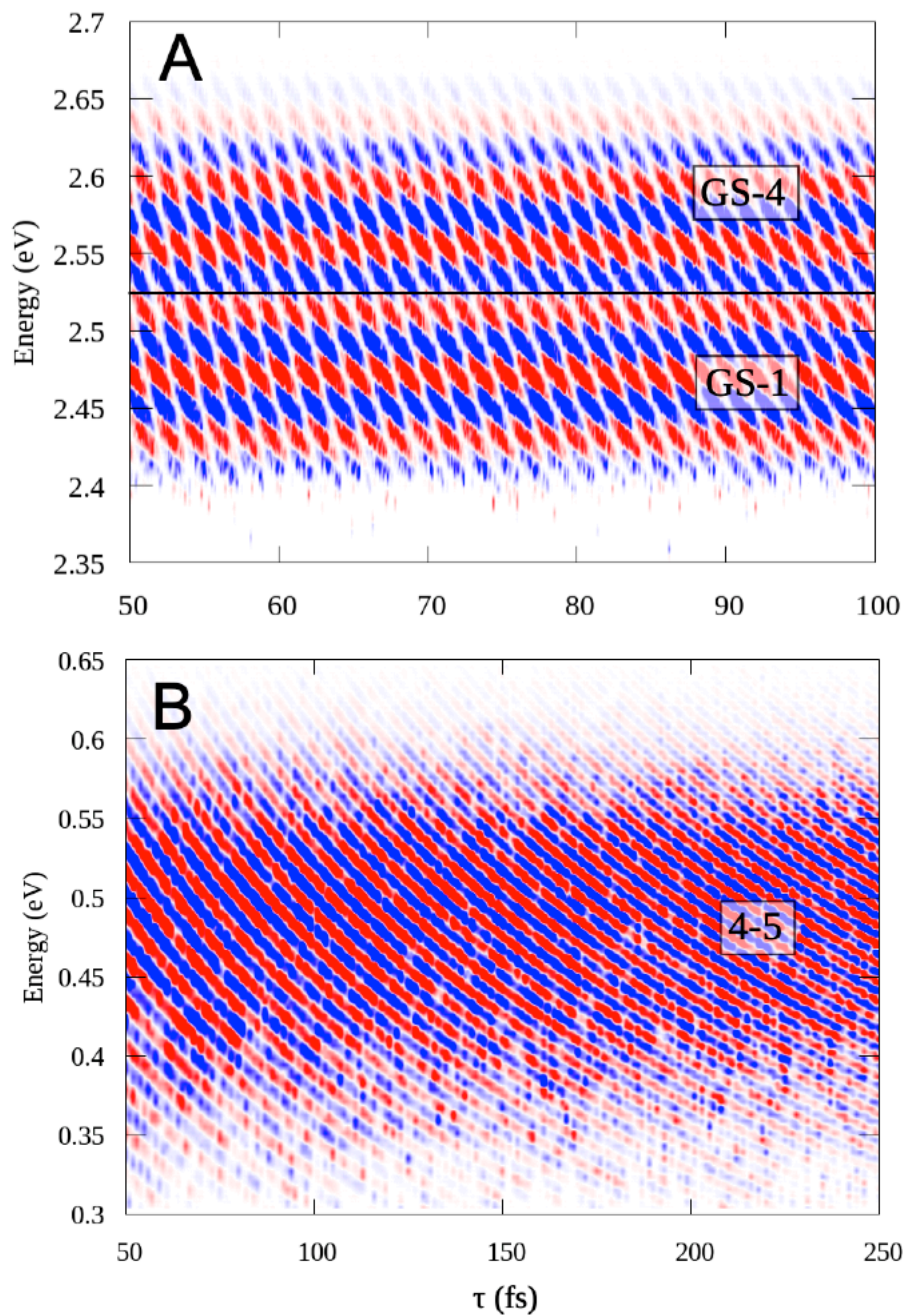


**Figure 8.** Heatmaps of the transient absorption spectra computed for the homodimer ( $D_A = D_B = 2.5$  nm,  $L = 0.55$  nm, 5% size dispersion). (A) GS to exciton spectral region ( $y$  axis range from 2.0 to 2.6 eV) computed for delay times corresponding to fast coherence beatings on 2 fs time scale and a pulse sequence VIS–VIS. In the case of the homodimer, the zero order label of the excitons is not relevant. The eigenexciton bands 1 and 4 are the two eigenstate bands resulting from the Coulomb coupling between the quasi degenerate zero order exciton bands on each dot:  $h1e_A$  and  $h1e_B$ . (B) The low frequency region of the  $y$  axis that is probed by the VIS–IR sequence of pulse, which probes the coherence between eigenexciton 4 and eigenexciton 5. The eigenexciton band 5 is the low eigenexciton band from by the Coulomb coupling between the  $h2e_A$  and  $h2e_B$  bands.

## 5. Conclusions

We have constructed a model of an excitonic dimer of QDs including both local and CT excitons that aimed at demonstrating the electronic coherence dynamics at the level of an ensemble that takes into account the inherent size dispersion of the individual QDs. Because of the inevitable size dispersion, each dimer is made of not exactly the same QDs, which leads to dispersion of the zero order exciton energies, Coulomb matrix elements, and transition dipoles. The size dispersion induces accidental resonances between the energy levels of the two QDs that can lead to a strong effective interdot coupling between local excitons; this is particularly the case when the excitonic bands are engineered to overlap by tuning the size of the QDs, with the largest effect being obtained in the case of a homodimer. We focused on dimers of small CdSe QDs, with diameters in the range of 2 to 4 nm. Provided that an accurate parametrization of the Hamiltonian is available, our approach is general and could be applied to other colloidal QDs.

Excitation by short fs pulses allows building superpositions of eigen excitons, which leads to interdot coherent energy transfer and charge migration. We show that the spectroscopic signature of excitonic coherence beatings is strong at the level of the ensemble and could be measured. Transition absorption spectra averaged over the ensemble allow probing two different time scales for the coherent beatings. These could also be probed using 2D electronic spectroscopy, as has already been done for solutions of isolated QDs [25,26,28–32]. The short few fs periods correspond to GS–exciton coherences, while the longer ones in the 10–20 fs range correspond to coherences between local excitons, which lead to charge migration and coherent energy transfer. There are also inter exciton coherences with much longer periods, in the range of dozens of fs. These inter exciton coherences will couple to the low frequency phonon and acoustic modes [24,82,83,88]. The large density of purely excitonic coherences occurring on a wide range of time scale can be controlled by selecting the mean size of the two QDs used to make the dimer. The ultrafast charge migration and interdot motion of the electronic density can be controlled by tuning the sequence of ultrashort fs laser pulses before the onset of dephasing owing to the coupling to the environment and to the phonon modes, opening the way to applications to light harvesting [12,13,89,90] and information processing devices [59,73,91].

**Supplementary Materials:** The following are available online at <http://www.mdpi.com/2076-3417/10/4/1328/s1>, Figure S1–Figure S13, Table S1.

**Author Contributions:** Conceptualization, F.R., H.G., B.F., and R.D.L.; methodology, F.R., H.G., B.F., and R.D.L.; software, H.G.; formal analysis, F.R., H.G., B.F., and R.D.L.; writing—original draft preparation, F.R. and H.G.; writing—review and editing, F.R., H.G., B.F., and R.D.L. All authors have read and agreed to the published version of the manuscript.

**Funding:** This work is supported by the FET open EC project COPAC #766563 and the Fonds National de la Recherche Scientifique (F.R.S-FNRS, Belgium), #T.0205.20. Computational resources have been provided by the Consortium des Equipements de Calcul Intensif (CECI), funded by the F.R.S.-FNRS under Grant #2.5020.11. B.F. acknowledges the support of the Ministero dell’Istruzione, Università e Ricerca through the grant Rita Levi Montalcini (2013).

**Conflicts of Interest:** The authors declare no conflict of interest.

## References

1. Alivisatos, A.P. Semiconductor Clusters, Nanocrystals, and Quantum Dots. *Science* **1996**, *271*, 933. [[CrossRef](#)]
2. Markovich, G.; Collier, C.P.; Henrichs, S.E.; Remacle, F.; Levine, R.D.; Heath, J.R. Architectonic Quantum Dot Solids. *Acc. Chem. Res.* **1999**, *32*, 415–423. [[CrossRef](#)]
3. Whetten, R.L.; Shafiqullin, M.N.; Khoury, J.T.; Schaaff, T.G.; Vezmar, I.; Alvarez, M.M.; Wilkinson, A. Crystal Structures of Molecular Gold Nanocrystal Arrays. *Acc. Chem. Res.* **1999**, *32*, 397–406. [[CrossRef](#)]
4. Murray, C.B.; Kagan, C.R.; Bawendi, M.G. Synthesis and Characterization of Monodisperse Nanocrystals and Close-Packed Nanocrystal Assemblies. *Ann. Rev. Mater. Sci.* **2000**, *30*, 545–610. [[CrossRef](#)]
5. Remacle, F.; Levine, R.D. Architecture with Designer Atoms: Simple Theoretical Considerations. *Proc. Natl. Acad. Sci. USA* **2000**, *97*, 553–558. [[CrossRef](#)]

6. *Nanocrystal Quantum Dots*, 2nd ed.; Klimov, V.I. (Ed.) CRC Press: Boca Raton, FL, USA, 2010.
7. Xu, X.; Stöttinger, S.; Battagliarin, G.; Hinze, G.; Mugnaioli, E.; Li, C.; Müllen, K.; Basché, T. Assembly and Separation of Semiconductor Quantum Dot Dimers and Trimers. *J. Am. Chem. Soc.* **2011**, *133*, 18062–18065. [[CrossRef](#)]
8. Williams, K.J.; Tisdale, W.A.; Leschkies, K.S.; Haugstad, G.; Norris, D.J.; Aydil, E.S.; Zhu, X.Y. Strong Electronic Coupling in Two-Dimensional Assemblies of Colloidal PbSe Quantum Dots. *ACS Nano* **2009**, *3*, 1532–1538. [[CrossRef](#)]
9. Koole, R.; Liljeroth, P.; de Mello Donegá, C.; Vanmaekelbergh, D.; Meijerink, A. Electronic Coupling and Exciton Energy Transfer in CdTe Quantum-Dot Molecules. *J. Am. Chem. Soc.* **2006**, *128*, 10436–10441. [[CrossRef](#)]
10. Cohen, E.; Komm, P.; Rosenthal-Strauss, N.; Dehnel, J.; Lifshitz, E.; Yochelis, S.; Levine, R.D.; Remacle, F.; Fresch, B.; Marcus, G.; et al. Fast Energy Transfer in CdSe Quantum Dot Layered Structures: Controlling Coupling with Covalent-Bond Organic Linkers. *J. Phys. Chem. C* **2018**, *122*, 5753–5758. [[CrossRef](#)]
11. Grimaldi, G.; Crisp, R.W.; ten Brinck, S.; Zapata, F.; van Ouwendorp, M.; Renaud, N.; Kirkwood, N.; Evers, W.H.; Kinge, S.; Infante, I.; et al. Hot-electron transfer in quantum-dot heterojunction films. *Nat. Commun.* **2018**, *9*, 2310. [[CrossRef](#)]
12. Kagan, C.R.; Lifshitz, E.; Sargent, E.H.; Talapin, D.V. Building devices from colloidal quantum dots. *Science* **2016**, *353*, aac5523. [[CrossRef](#)] [[PubMed](#)]
13. Talapin, D.V.; Lee, J.-S.; Kovalenko, M.V.; Shevchenko, E.V. Prospects of Colloidal Nanocrystals for Electronic and Optoelectronic Applications. *Chem. Rev.* **2010**, *110*, 389–458. [[CrossRef](#)] [[PubMed](#)]
14. Panfil, Y.E.; Oded, M.; Banin, U. Colloidal Quantum Nanostructures: Emerging Materials for Display Applications. *Angew. Chem. Int. Ed.* **2018**, *57*, 4274–4295. [[CrossRef](#)] [[PubMed](#)]
15. Murray, C.B.; Norris, D.J.; Bawendi, M.G. Synthesis and characterization of nearly monodisperse CdE (E = sulfur, selenium, tellurium) semiconductor nanocrystallites. *J. Am. Chem. Soc.* **1993**, *115*, 8706–8715. [[CrossRef](#)]
16. Kagan, C.R.; Murray, C.B.; Nirmal, M.; Bawendi, M.G. Electronic Energy Transfer in CdSe Quantum Dot Solids. *Phys. Rev. Lett.* **1996**, *76*, 1517–1520. [[CrossRef](#)]
17. Norris, D.J.; Bawendi, M.G. Measurement and assignment of the size-dependent optical spectrum in CdSe quantum dots. *Phys. Rev. B* **1996**, *53*, 16338–16346. [[CrossRef](#)]
18. Efros, A.L.; Rosen, M.; Kuno, M.; Nirmal, M.; Norris, D.J.; Bawendi, M. Band-edge exciton in quantum dots of semiconductors with a degenerate valence band: Dark and bright exciton states. *Phys. Rev. B* **1996**, *54*, 4843–4856. [[CrossRef](#)]
19. Soloviev, V.N.; Eichhöfer, A.; Fenske, D.; Banin, U. Size-Dependent Optical Spectroscopy of a Homologous Series of CdSe Cluster Molecules. *J. Am. Chem. Soc.* **2001**, *123*, 2354–2364. [[CrossRef](#)]
20. Sercel, P.C.; Efros, A.L. Band-Edge Exciton in CdSe and Other II–VI and III–V Compound Semiconductor Nanocrystals—Revisited. *Nano Lett.* **2018**, *18*, 4061–4068. [[CrossRef](#)]
21. Sercel, P.C.; Shabaev, A.; Efros, A.L. Photoluminescence Enhancement through Symmetry Breaking Induced by Defects in Nanocrystals. *Nano Lett.* **2017**, *17*, 4820–4830. [[CrossRef](#)]
22. Ma, H.; Jin, Z.; Zhang, Z.; Li, G.; Ma, G. Exciton Spin Relaxation in Colloidal CdSe Quantum Dots at Room Temperature. *J. Phys. Chem. A* **2012**, *116*, 2018–2023. [[CrossRef](#)] [[PubMed](#)]
23. Moreels, I.; Rainò, G.; Gomes, R.; Hens, Z.; Stöferle, T.; Mahrt, R.F. Band-Edge Exciton Fine Structure of Small, Nearly Spherical Colloidal CdSe/ZnS Quantum Dots. *ACS Nano* **2011**, *5*, 8033–8039. [[CrossRef](#)] [[PubMed](#)]
24. Huxter, V.M.; Scholes, G.D. Acoustic phonon strain induced mixing of the fine structure levels in colloidal CdSe quantum dots observed by a polarization grating technique. *J. Chem. Phys.* **2010**, *132*, 104506. [[CrossRef](#)] [[PubMed](#)]
25. Caram, J.R.; Zheng, H.; Dahlberg, P.D.; Rolczynski, B.S.; Griffin, G.B.; Fidler, A.F.; Dolzhenkov, D.S.; Talapin, D.V.; Engel, G.S. Persistent Interexcitonic Quantum Coherence in CdSe Quantum Dots. *J. Phys. Chem. Lett.* **2014**, *5*, 196–204. [[CrossRef](#)] [[PubMed](#)]
26. Caram, J.R.; Zheng, H.; Dahlberg, P.D.; Rolczynski, B.S.; Griffin, G.B.; Dolzhenkov, D.S.; Talapin, D.V.; Engel, G.S. Exploring size and state dynamics in CdSe quantum dots using two-dimensional electronic spectroscopy. *J. Chem. Phys.* **2014**, *140*, 084701. [[CrossRef](#)] [[PubMed](#)]
27. Dong, S.; Trivedi, D.; Chakraborty, S.; Kobayashi, T.; Chan, Y.; Prezhdo, O.V.; Loh, Z.-H. Observation of an Excitonic Quantum Coherence in CdSe Nanocrystals. *Nano Lett.* **2015**, *15*, 6875–6882. [[CrossRef](#)]

28. Janke, E.M.; Williams, N.E.; She, C.; Zherebetsky, D.; Hudson, M.H.; Wang, L.; Gosztola, D.J.; Schaller, R.D.; Lee, B.; Sun, C.; et al. Origin of Broad Emission Spectra in InP Quantum Dots: Contributions from Structural and Electronic Disorder. *J. Am. Chem. Soc.* **2018**, *140*, 15791–15803. [CrossRef]
29. Cassette, E.; Pensack, R.D.; Mahler, B.; Scholes, G.D. Room-temperature exciton coherence and dephasing in two-dimensional nanostructures. *Nat. Commun.* **2015**, *6*, 6086. Available online: <https://www.nature.com/articles/ncomms7086#supplementary-information> (accessed on 15 January 2015). [CrossRef]
30. Wong, C.Y.; Scholes, G.D. Biexcitonic Fine Structure of CdSe Nanocrystals Probed by Polarization-Dependent Two-Dimensional Photon Echo Spectroscopy. *J. Phys. Chem. A* **2011**, *115*, 3797–3806. [CrossRef]
31. Turner, D.B.; Hassan, Y.; Scholes, G.D. Exciton Superposition States in CdSe Nanocrystals Measured Using Broadband Two-Dimensional Electronic Spectroscopy. *Nano Lett.* **2012**, *12*, 880–886. [CrossRef]
32. Collini, E.; Gattuso, H.; Bolzonello, L.; Casotto, A.; Volpato, A.; Dibeneditto, C.N.; Fanizza, E.; Striccoli, M.; Remacle, F. Quantum Phenomena in Nanomaterials: Coherent Superpositions of Fine Structure States in CdSe Nanocrystals at Room Temperature. *J. Phys. Chem. C* **2019**. [CrossRef]
33. Klimov, V.I.; McBranch, D.W.; Leatherdale, C.A.; Bawendi, M.G. Electron and hole relaxation pathways in semiconductor quantum dots. *Phys. Rev. B* **1999**, *60*, 13740–13749. [CrossRef]
34. Klimov, V.I. Mechanisms for Photogeneration and Recombination of Multiexcitons in Semiconductor Nanocrystals: Implications for Lasing and Solar Energy Conversion. *J. Phys. B* **2006**, *110*, 16827–16845.
35. Mlinar, V.; Zunger, A. Internal electronic structure and fine structure of multiexcitons in semiconductor quantum dots. *Phys. Rev. B* **2009**, *80*, 205311. [CrossRef]
36. Sewall, S.L.; Franceschetti, A.; Cooney, R.R.; Zunger, A. Direct observation of the structure of band-edge biexcitons in colloidal semiconductor CdSe quantum dots. *Phys. Rev. B* **2009**, *80*, 081310. [CrossRef]
37. Trivedi, D.J.; Wang, L.; Prezhdo, O.V. Auger-Mediated Electron Relaxation Is Robust to Deep Hole Traps: Time-Domain Ab Initio Study of CdSe Quantum Dots. *Nano Lett.* **2015**, *15*, 2086–2091. [CrossRef]
38. Morgan, N.Y.; Leatherdale, C.A.; Drndić, M.; Jarosz, M.V.; Kastner, M.A.; Bawendi, M. Electronic transport in films of colloidal CdSe nanocrystals. *Phys. Rev. B* **2002**, *66*, 075339. [CrossRef]
39. Liang, Y.; Thorne, J.E.; Parkinson, B.A. Controlling the Electronic Coupling between CdSe Quantum Dots and Thiol Capping Ligands via pH and Ligand Selection. *Langmuir* **2012**, *28*, 11072–11077. [CrossRef]
40. Ginger, D.S.; Greenham, N.C. Charge injection and transport in films of CdSe nanocrystals. *J. Appl. Phys.* **2000**, *87*, 1361–1368. [CrossRef]
41. Lee, J.-S.; Kovalenko, M.V.; Huang, J.; Chung, D.S.; Talapin, D.V. Band-like transport, high electron mobility and high photoconductivity in all-inorganic nanocrystal arrays. *Nat. Nanotechnol.* **2011**, *6*, 348. Available online: <https://www.nature.com/articles/nnano.2011.46#supplementary-information> (accessed on 24 April 2011). [CrossRef]
42. Brus, L.E. Electron–electron and electron-hole interactions in small semiconductor crystallites: The size dependence of the lowest excited electronic state. *J. Chem. Phys.* **1984**, *80*, 4403–4409. [CrossRef]
43. Wang, Y.; Herron, N. Nanometer-sized semiconductor clusters: Materials synthesis, quantum size effects, and photophysical properties. *J. Phys. Chem.* **1991**, *95*, 525–532. [CrossRef]
44. Koole, R.; Groeneveld, E.; Vanmaekelbergh, D.; Meijerink, A.; deMelloDonega, C. Size Effect on Semiconductor Nanoparticles. In *Nanoparticles*; deMelloDonega, C., Ed.; Springer: Berlin, Germany, 2014.
45. Zunger, A. Electronic Structure Theory of Semiconductor Quantum Dots. *MRS Bull.* **1998**, *23*, 35–42. [CrossRef]
46. Prezhdo, O.V. Photoinduced Dynamics in Semiconductor Quantum Dots: Insights from Time-Domain ab Initio Studies. *Acc. Chem. Res.* **2009**, *42*, 2005–2016. [CrossRef]
47. Wang, L.-W.; Zunger, A. Pseudopotential calculations of nanoscale CdSe quantum dots. *Phys. Rev. B* **1996**, *53*, 9579–9582. [CrossRef]
48. Wang, Z.A. High-Energy Excitonic Transitions in CdSe Quantum Dots. *J. Phys. Chem. B* **1998**, *102*, 6449–6454. [CrossRef]
49. Wang, Y.; Liu, Y.-H.; Zhang, Y.; Kowalski, P.J.; Rohrs, H.W.; Buhro, W.E. Preparation of Primary Amine Derivatives of the Magic-Size Nanocluster (CdSe)<sub>13</sub>. *Inorg. Chem.* **2013**, *52*, 2933–2938. [CrossRef]
50. Vogl, P.; Hjalmarsen, H.P.; Dow, J.D. A semi-empirical tight-binding theory of the electronic structure of semiconductors. *J. Phys. Chem. Sol.* **1983**, *44*, 365–378. [CrossRef]

51. Klimeck, G.; Oyafuso, F.; Boykin, T.B.; Bowen, R.C.; Allmen, P.V. Development of a Nanoelectronic 3-D (NEMO 3-D) Simulator for Multimillion Atom Simulations and Its Application to Alloyed Quantum Dots. *CMES* **2002**, *3*, 602–642.
52. Lee, S.; Jönsson, L.; Wilkins, J.W.; Bryant, G.W.; Klimeck, G. Electron-hole correlations in semiconductor quantum dots with tight-binding wave functions. *Phys. Rev. B* **2001**, *63*, 195318. [[CrossRef](#)]
53. Kilina, S.V.; Kilin, D.S.; Prezhdo, O.V. Breaking the Phonon Bottleneck in PbSe and CdSe Quantum Dots: Time-Domain Density Functional Theory of Charge Carrier Relaxation. *ACS Nano* **2009**, *3*, 93–99. [[CrossRef](#)] [[PubMed](#)]
54. Pal, S.; Trivedi, D.J.; Akimov, A.V.; Aradi, B.; Frauenheim, T.; Prezhdo, O.V. Nonadiabatic Molecular Dynamics for Thousand Atom Systems: A Tight-Binding Approach toward PYXAID. *J. Chem. Theory Comput.* **2016**, *12*, 1436–1448. [[CrossRef](#)] [[PubMed](#)]
55. Luttinger, J.M.; Kohn, W. Motion of Electrons and Holes in Perturbed Periodic Fields. *Phys. Rev.* **1955**, *97*, 869–883. [[CrossRef](#)]
56. Brus, L. Electronic wave functions in semiconductor clusters: Experiment and theory. *J. Phys. Chem.* **1986**, *90*, 2555–2560. [[CrossRef](#)]
57. Efros, A.L. Luminescence polarization of CdSe microcrystals. *Phys. Rev. B* **1992**, *46*, 7448–7458. [[CrossRef](#)]
58. Efros, A.L.; Rosen, M. The electronic structure of semi-conducting nanocrystal. *Ann. Rev. Mater. Sci.* **2000**, *30*, 475–521. [[CrossRef](#)]
59. Lovett, B.W.; Reina, J.H.; Nazir, A.; Briggs, G.A.D. Optical schemes for quantum computation in quantum dot molecules. *Phys. Rev. B* **2003**, *68*, 205319. [[CrossRef](#)]
60. Nazir, A.; Lovett, B.W.; Barrett, S.D.; Reina, J.H.; Briggs, G.A.D. Anticrossings in Förster coupled quantum dots. *Phys. Rev. B* **2005**, *71*, 045334. [[CrossRef](#)]
61. Kruchinin, S.Y.; Fedorov, A.V.; Baranov, A.V.; Perova, T.S.; Berwick, K. Resonant energy transfer in quantum dots: Frequency-domain luminescent spectroscopy. *Phys. Rev. B* **2008**, *78*, 125311. [[CrossRef](#)]
62. Kruchinin, S.Y.; Fedorov, A.V.; Baranov, A.V.; Perova, T.S.; Berwick, K. Electron-electron scattering in a double quantum dot: Effective mass approach. *J. Chem. Phys.* **2010**, *133*, 104704. [[CrossRef](#)]
63. Troiani, F.; Hohenester, U.; Molinari, E. Electron-hole localization in coupled quantum dots. *Phys. Rev. B* **2002**, *65*, 161301. [[CrossRef](#)]
64. Seibt, J.; Pullerits, T. Beating Signals in 2D Spectroscopy: Electronic or Nuclear Coherences? Application to a Quantum Dot Model System. *J. Phys. Chem. C* **2013**, *117*, 18728–18737. [[CrossRef](#)]
65. Seibt, J.; Hansen, T.; Pullerits, T. 3D Spectroscopy of Vibrational Coherences in Quantum Dots: Theory. *J. Phys. Chem. B* **2013**, *117*, 11124–11133. [[CrossRef](#)] [[PubMed](#)]
66. Karki, K.J.; Ma, F.; Zheng, K.; Zidek, K.; Mousa, A.; Abdellah, M.A.; Messing, M.E.; Wallenberg, L.R.; Yartsev, A.; Pullerits, T. Multiple exciton generation in nano-crystals revisited: Consistent calculation of the yield based on pump-probe spectroscopy. *Sci. Rep.* **2013**, *3*, 2287. [[CrossRef](#)]
67. Wang, H.; de Mello Donegá, C.; Meijerink, A.; Glasbeek, M. Ultrafast Exciton Dynamics in CdSe Quantum Dots Studied from Bleaching Recovery and Fluorescence Transients. *J. Phys. Chem. B* **2006**, *110*, 733–737. [[CrossRef](#)]
68. Kambhampati, P. Hot Exciton Relaxation Dynamics in Semiconductor Quantum Dots: Radiationless Transitions on the Nanoscale. *J. Phys. Chem. C* **2011**, *115*, 22089–22109. [[CrossRef](#)]
69. Židek, K.; Zheng, K.; Ponseca, C.S.; Messing, M.E.; Wallenberg, L.R.; Chábera, P.; Abdellah, M.; Sundström, V.; Pullerits, T. Electron Transfer in Quantum-Dot-Sensitized ZnO Nanowires: Ultrafast Time-Resolved Absorption and Terahertz Study. *J. Am. Chem. Soc.* **2012**, *134*, 12110–12117. [[CrossRef](#)]
70. Walsh, B.R.; Sonnichsen, C.; Mack, T.G.; Saari, J.I.; Krause, M.M.; Nick, R.; Coe-Sullivan, S.; Kambhampati, P. Excited State Phononic Processes in Semiconductor Nanocrystals Revealed by Excitonic State-Resolved Pump/Probe Spectroscopy. *J. Phys. Chem. C* **2019**, *123*, 3868–3875. [[CrossRef](#)]
71. Scholes, G.D. Coherence from Light Harvesting to Chemistry. *J. Phys. Chem. Lett.* **2018**, *9*, 1568–1572. [[CrossRef](#)]
72. Fresch, B.; Cipolloni, M.; Yan, T.-M.; Collini, E.; Levine, R.D.; Remacle, F. Parallel and Multivalued Logic by the Two-Dimensional Photon-Echo Response of a Rhodamine–DNA Complex. *J. Phys. Chem. Lett.* **2015**, *6*, 1714–1718. [[CrossRef](#)]
73. Fresch, B.; Hiluf, D.; Collini, E.; Levine, R.D.; Remacle, F. Molecular decision trees realized by ultrafast electronic spectroscopy. *Proc. Natl. Acad. Sci. USA* **2013**, *110*, 17183–17188. [[CrossRef](#)] [[PubMed](#)]

74. Fu, H.; Wang, L.-W.; Zunger, A. Excitonic exchange splitting in bulk semiconductors. *Phys. Rev. B* **1999**, *59*, 5568–5574. [[CrossRef](#)]
75. Wang, L.-W.; Zunger, A. Local-density-derived semiempirical pseudopotentials. *Phys. Rev. B* **1995**, *51*, 17398–17416. [[CrossRef](#)] [[PubMed](#)]
76. Kelley, A.M. Electron–Phonon Coupling in CdSe Nanocrystals from an Atomistic Phonon Model. *ACS Nano* **2011**, *5*, 5254–5262. [[CrossRef](#)] [[PubMed](#)]
77. Knox, R.S. *Solid State Physics*; Academic: New York, NY, USA, 1963; Volume 5.
78. Franceschetti, A.; Fu, H.; Wang, L.W.; Zunger, A. Many-body pseudopotential theory of excitons in InP and CdSe quantum dots. *Phys. Rev. B* **1999**, *60*, 1819–1829. [[CrossRef](#)]
79. Ferreyra, J.M.; Proetto, C.R. Quantum size effects on excitonic Coulomb and exchange energies in finite-barrier semiconductor quantum dots. *Phys. Rev. B* **1999**, *60*, 10672–10675. [[CrossRef](#)]
80. Specht, J.F.; Knorr, A.; Richter, M. Two-dimensional spectroscopy: An approach to distinguish Förster and Dexter transfer processes in coupled nanostructures. *Phys. Rev. B* **2015**, *91*, 155313. [[CrossRef](#)]
81. Akimov, A.V.; Prezhdo, O.V. Large-Scale Computations in Chemistry: A Bird’s Eye View of a Vibrant Field. *Chem. Rev.* **2015**, *115*, 5797–5890. [[CrossRef](#)]
82. Kelley, A.M. Electron–Phonon Coupling in CdSe Nanocrystals. *J. Phys. Chem. Lett.* **2010**, *1*, 1296–1300. [[CrossRef](#)]
83. Salvador, M.R.; Graham, M.W.; Scholes, G.D. Exciton-phonon coupling and disorder in the excited states of CdSe colloidal quantum dots. *J. Chem. Phys.* **2006**, *125*, 184709. [[CrossRef](#)]
84. Klimov, V.I. Optical Nonlinearities and Ultrafast Carrier Dynamics in Semiconductor Nanocrystals. *J. Phys. Chem. B* **2000**, *104*, 6112–6123. [[CrossRef](#)]
85. Crooker, S.A.; Hollingsworth, J.A.; Tretiak, S.; Klimov, V.I. Spectrally Resolved Dynamics of Energy Transfer in Quantum-Dot Assemblies: Towards Engineered Energy Flows in Artificial Materials. *Phys. Rev. Lett.* **2002**, *89*, 186802. [[CrossRef](#)] [[PubMed](#)]
86. Seidner, L.; Stock, G.; Domcke, W. Nonperturbative approach to femtosecond spectroscopy: General theory and application to multidimensional nonadiabatic photoisomerization processes. *J. Chem. Phys.* **1995**, *103*, 3998–4011. [[CrossRef](#)]
87. Mengxi, W.; Shaohao, C.; Seth, C.; Kenneth, J.S.; Mette, B.G. Theory of strong-field attosecond transient absorption. *J. Phys. B* **2016**, *49*, 062003.
88. Lin, C.; Gong, K.; Kelley, D.F.; Kelley, A.M. Size-Dependent Exciton–Phonon Coupling in CdSe Nanocrystals through Resonance Raman Excitation Profile Analysis. *J. Phys. Chem. C* **2015**, *119*, 7491–7498. [[CrossRef](#)]
89. Chistyakov, A.A.; Zvaigzne, M.A.; Nikitenko, V.R.; Tameev, A.R.; Martynov, I.L.; Prezhdo, O.V. Optoelectronic Properties of Semiconductor Quantum Dot Solids for Photovoltaic Applications. *J. Phys. Chem. Lett.* **2017**, *8*, 4129–4139. [[CrossRef](#)] [[PubMed](#)]
90. Hu, Z.; Engel, G.S.; Kais, S. Double-excitation manifold’s effect on exciton transfer dynamics and the efficiency of coherent light harvesting. *Phys. Chem. Chem. Phys.* **2018**, *20*, 30032–30040. [[CrossRef](#)]
91. Yan, T.-M.; Fresch, B.; Levine, R.D.; Remacle, F. Information processing in parallel through directionally resolved molecular polarization components in coherent multidimensional spectroscopy. *J. Chem. Phys.* **2015**, *143*, 064106. [[CrossRef](#)]

